J. Fluid Mech. (1984), *vol.* 148, *pp.* 413–442
Printed in Great Britain

Final stages of transition to turbulence in plane channel flow

By S. BIRINGEN

Department of Mechanical Engineering, University of New Hampshire, Durham, New Hampshire 03824

(Received 12 July 1982 and in revised form 6 June 1984)

This paper involves a numerical simulation of the final stages of transition to turbulence in plane channel flow at a Reynolds number of 1500. Three-dimensional incompressible Navier–Stokes equations are numerically integrated to obtain the time evolution of two- and three-dimensional finite-amplitude disturbances. Computations are performed on the CYBER-203 vector processor for a $32 \times 51 \times 32$ grid. Solutions indicate the existence of structures similar to those observed in the laboratory and characteristic of the various stages of transition that lead to final breakdown. In particular, evidence points to the formation of a Λ-shaped vortex and the subsequent system of horsehoe vortices inclined to the main flow direction as the primary elements of transition. Details of the resulting flow field after breakdown indicate the evolution of streaklike formations found in turbulent flows. Although the flow field does approach a steady state (turbulent channel flow), the introduction of subgrid-scale terms seems necessary to obtain fully developed turbulence statistics.

1. Introduction

Recent experiments by Nishioka, Asai & Iida (1981) have shown that transition to turbulence in plane channel flow follows a sequence of events similar to that observed by Klebanoff, Tidstrom & Sargent (1962) in the boundary-layer transition. In this work, a direct numerical integration of the Navier–Stokes equations is performed in an attempt to simulate these events in plane channel flow, during the later stages of transition.

In their experiments, Nishioka *et al.* (1981) used a vibrating ribbon technique to generate two-dimensional disturbances fixed at 72 Hz to excite the fully developed flow in a channel with a 27.4 aspect ratio. They measured the streamwise mean and fluctuating velocities, U_1 and u_1' respectively, at a fixed streamwise location at a subcritical (linearly stable) Reynolds number $Re = 5000$, and simulated the various stages of transition by varying the disturbance amplitude. Their observations show that subcritical instability takes place at a threshold amplitude of $(u_1')_{\max}/U_0 = 0.01$, where U_0 is the mean velocity at the channel centreline. The evolution of this instability is evidenced by the intensification of the spanwise variation of the wavefront, which develops into a peak–valley structure. Nishioka *et al.* (1981) observed that the flow development then follows a trend which is similar to transition in the boundary layer (Klebanoff *et al.* 1962; Kovasznay, Komoda & Vasudeva 1962): local shear layers are formed away from the wall at spanwise peak positions ($u_1'/U_0 = 0.06$); these shear layers start to exhibit a 'kink', which is the manifestation of secondary instability and is accompanied by a 'spike' in the u_1' signal

($u_1'/U_0 = 0.11$). In rapid succession, two-, three-, five-, and multispike stages are observed with increasing amplitude of the primary disturbance. Nishioka *et al.* (1981) present evidence that in the final stages of transition the flow starts to develop structures very similar to those found in fully developed wall turbulence. During this stage the flow field is characterized by the development of a viscous sublayer, occurrence of the typical 'streaks' close to the wall, and the formation of horseshoe vortices sometimes referred to as the building blocks of wall turbulence (Theodorsen 1954). The present work attempts to simulate this sequence of events.

Direct numerical integrations of the Navier–Stokes equations for the simulation of channel-flow transition has been the subject of some previous investigations. George & Hellums (1972) and Fasel, Bestek & Schefenacker (1977) used the two-dimensional Navier–Stokes equations to investigate the stability of channel flow to two-dimensional finite-amplitude disturbances. George & Hellums studied the relationship between critical amplitude and Reynolds number and found a minimum Reynolds number $Re = 3500$ below which their predictions remained stable. This is contrary to experimental evidence (e.g. Kao & Park 1970), which indicates instability of plane channel flow to finite-amplitude disturbances at Reynolds numbers as low as 1000. Fasel *et al.* investigated the effects of disturbance amplitude on transition at subcritical and supercritical Reynolds numbers. They found that increasing amplitude ($u_1'/U_0 = 0.06$) of two-dimensional disturbances can drive plane channel flow to instability at a subcritical Reynolds number $Re = 5000$. Although some insight into finite-amplitude instability of two-dimensional disturbances can be obtained from such calculations, a proper simulation of the transition process requires the use of the three-dimensional Navier–Stokes equations. Once the process extends into the nonlinear regime, transition becomes increasingly three-dimensional, so that, for a realistic (physically plausible) representation of flow breakdown, spanwise variations of the flow-field variables must be accounted for. It is also well known that creation of vorticity through vortex stretching, an essential ingredient of transition, can take place only in a three-dimensional flow field. Hence numerical solutions of the two-dimensional Navier–Stokes equations cannot represent energy transfer down the wavenumber spectrum, which is the basic mechanism of laminar-flow transition to turbulence and the result of the vortex-stretching mechanism.

Effects of three-dimensionality on transition have first been documented in detail by Klebanoff *et al.* (1962). Accordingly, three-dimensionality manifests itself mainly in the spanwise velocity variations, resulting in the production of streamwise vorticity, which in turn interacts with the spanwise vorticity and drives the flow to breakdown. Orszag & Kells (1980) and Orszag & Patera (1981) have expanded on this idea and studied the susceptibility of plane channel flow to three-dimensional disturbances by numerically integrating the three-dimensional Navier–Stokes equations. Their computations at subcritical Reynolds numbers revealed some interesting aspects of subcritical transition. They found that initial disturbances, which are finite-amplitude two-dimensional Orr–Sommerfeld eigensolutions, decay slowly, and, as expected, the rate of decay increases with decreasing Reynolds number. They also found that the addition of three-dimensional finite-amplitude disturbances promotes rapid instability at Reynolds numbers as low as 1000, which is in good agreement with the experiments of Kao & Park (1970). Their results suggest a similar tendency of the flow to instability even for small-amplitude three-dimensional disturbances. They conclude that the mechanism that drives plane channel flow to instability is the interaction of two-dimensional and three-dimensional disturbances, supporting the idea that three-dimensionality is central to transition in plane channel flow. More

recently, Kleiser (1982) incorporated a spectral method to solve the three-dimensional Navier–Stokes equations starting with weakly three-dimensional initial conditions. Comparisons of his results with the experiments of Nishioka, Asai & Iida (1980) up to the first-spike stage are favourable even from a quantitative point of view, supporting the idea that direct numerical simulations can be used as a means of investigating the nonlinear transition process.

In spite of the accumulation of theoretical and experimental information on transition, ambiguities still remain concerning the nature of nonlinear mechanisms prior to breakdown. The relation between streamwise vortices and spanwise vorticity is one such area that deserves attention. Based on Theodorsen's (1954) vortex model, experimental observations of Hama & Nutant (1963) in a transitional boundary layer and recent flow-visualization studies (Head & Bandyopadhyay 1981; Perry, Lim & Teh 1981; Smith & Schwartz 1983), streamwise and spanwise vorticity can be viewed as parts of a vortex loop that evolves into a horseshoe vortex during the final stages of transition. This view implies that streamwise vortices *originate* from the vortex-shedding mechanism owing to the nonlinear distortions of the initially two-dimensional spanwise vorticity. In contrast, according to the Benney–Lin (1960) theory, nonlinear distortions of the wavefront are *initiated* by a pair of counterrotating streamwise vortices which are present in the flow field. In addition to this problem, other essential queries concerning the mechanism of generation of a turbulent spot and its relation to wall turbulence remain as areas that need further study.

It can be conjectured from the above discussion that our understanding of nonlinear mechanisms of transition and breakdown is not yet complete. The necessity of further work in this direction is especially apparent in channel-flow transition, for which detailed information on the final stages of transition is scarce apart from the experiments of Nishioka *et al.* (1981). The present work addresses this aspect of transition in channel flow. For a realistic representation of the underlying physical phenomena, the full three-dimensional time-dependent Navier–Stokes equations were employed in this work. Calculations were performed at a linearly stable Reynolds number ($Re = 1500$), with finite-amplitude two- and three-dimensional eigensolutions of the Orr–Sommerfeld equation used as the initial conditions. No attempt was made herein to study the effects of different initial conditions or of Reynolds numbers; this is the subject of another investigation.

In §2 of this paper the numerical methods used in this study are briefly discussed. In §3 results of calculations are presented, and, whenever possible, the evolution of the computed flow field is compared with the experiments of Nishioka *et al.* (1981). Finally, §4 contains a summary of results and some concluding remarks.

2. The calculation procedure

The calculation procedure is based on the imcompressible Navier–Stokes equations in primitive-variable form,

$$\frac{\partial u_i}{\partial t} + u_l \frac{\partial u_i}{\partial x_l} = -\frac{1}{\rho}\frac{\partial p'}{\partial x_i} + \nu \frac{\partial^2 u_i}{\partial x_l \partial x_l}, \tag{1}$$

and the continuity equation,

$$\frac{\partial u_i}{\partial x_i} = 0, \tag{2}$$

where u_i are the velocities along the x_i directions, ρ is the density, ν is the kinematic viscosity and p' is the total hydrostatic pressure. The equations are non-

dimensionalized by the mean centreline velocity U_0 and the channel half-width h. The flow is assumed to be driven by a constant mean pressure gradient $2/Re$, where $Re = u_0 h/\nu$ is the Reynolds number. Also, the convective terms are written in a form that prevents occurrence of nonlinear instability in the numerical solution procedure by ensuring conservation of momentum and energy (Mansour, Ferziger & Reynolds 1978). The final form of the Navier–Stokes equations reads

$$\frac{\partial u_i}{\partial t} + u_l\left(\frac{\partial u_i}{\partial x_l} - \frac{\partial u_l}{\partial x_i}\right) = -\frac{\partial P}{\partial x_i} + \frac{2}{Re}\delta_{il} + \frac{1}{Re}\frac{\partial^2 u_i}{\partial x_l \partial x_l}, \tag{3}$$

where $P = p'/\rho + \frac{1}{2}u_l u_l$ is the pressure head and δ_{il} is the Kronecker delta.

The flow is assumed to be periodic in the streamwise x_1 and the spanwise x_3 directions, along which the flow-field variables can be expanded in terms of Fourier series. This enables the use of the pseudospectral method (Orszag 1972) to calculate the spatial derivatives along x_1 and x_3 by use of discrete Fourier transforms. Considering transforms in the x_1 direction, along which there are N_1 equally spaced mesh points, the velocity component u_1 can be written as

$$u_1(x_1) = \sum_{n_1 = -\frac{1}{2}N_1}^{\frac{1}{2}N_1 - 1} \hat{u}_1(k_1)\, \mathrm{e}^{\mathrm{i}k_1 x_1}, \tag{4}$$

where $x_1 = m\,\Delta x_1$ $(m = 0, 1, \ldots, N_1 - 1)$ and $k_1 = 2\pi n_1/N_1\,\Delta x_1$. Accordingly, the Fourier transform of u_1 is

$$\hat{u}_1(k_1) = \frac{1}{N_1}\sum_{m=0}^{N_1 - 1} u_1(x_1)\, \mathrm{e}^{-\mathrm{i}k_1 x_1}. \tag{5}$$

The spatial derivative of u_1 along x_1 can now be written as

$$\frac{\partial u_1(x_1)}{\partial x_1} = \sum_{n_1 = -\frac{1}{2}N_1}^{\frac{1}{2}N_1 - 1} \mathrm{i}k_1\, \hat{u}_1(k_1)\, \mathrm{e}^{\mathrm{i}k_1 x_1}. \tag{6}$$

The derivative can be computed by forming the Fourier transform of $u_1(x_1)$, multiplying the result by ik_1 and computing the inverse transform. For periodic functions the pseudospectral method provides a means by which the spatial derivatives are evaluated with maximum accuracy for a given number of grid points. Along the x_2 direction a mesh stretching that concentrates grid points close to the solid walls is employed (Moin, Reynolds & Ferziger 1978). The resulting mesh enables the resolution of the sublayer that is formed during transition for $y^+ < 2$, where y^+ is the coordinate along x_2, in wall units. Spatial derivatives along x_2 are evaluated by a second-order finite-difference scheme on this non-uniform mesh.

The governing equations were numerically integrated by the semi-implicit method of Moin *et al.* (1978). This procedure employs the explicit Adams–Bashforth method for the convective terms and the implicit Crank–Nicolson method for pressure and for the viscous-diffusion terms, so that the method is second-order accurate both in space and time. In order to start the two-time-level Adams–Bashforth method, the Euler-implicit method is used at the first time step.

Once the governing equations are discretized in time, a two-dimensional Fourier transform along the periodic directions x_1 and x_3 transforms the equations into the (k_1, k_3) wavenumber space. The transformed equations are written below in block-tridiagonal form for inversion along x_2:

$$\boldsymbol{A}\boldsymbol{F}_{j+1}^{n+1} + \boldsymbol{B}\boldsymbol{F}_{j}^{n+1} + \boldsymbol{C}\boldsymbol{F}_{j-1}^{n+1} = \boldsymbol{R}_j^n. \tag{7}$$

In (7), $\boldsymbol{A}$, $\boldsymbol{B}$, and $\boldsymbol{C}$ are coefficient matrices, $\boldsymbol{F}_j^{n+1}$ is the solution vector at the advanced time level $n+1$ and at the x_2 directional node j; $\boldsymbol{R}_j^n$ is the right-hand-side vector

that contains the convective, diffusive and pressure terms at the previous time levels. These are given as

$$\boldsymbol{F} = \begin{bmatrix} \hat{u}_1 \\ \hat{u}_2 \\ \hat{u}_3 \\ \hat{p} \end{bmatrix}, \quad \boldsymbol{A} = \begin{bmatrix} C2_j & 0 & 0 & 0 \\ 0 & C2_j & 0 & 0 \\ 0 & 0 & C1_j & 0 \\ 0 & 0 & C2_j & -ReC1_j \end{bmatrix},$$

$$\boldsymbol{B} = \begin{bmatrix} B2j-\phi & 0 & 0 & \pm(k_1)_j Re \\ 0 & B2_j-\phi & 0 & \pm(k_3)_j Re \\ \mp(k_1)_j & \mp(k_3)_j & B1_j & 0 \\ 0 & 0 & B2_j-\phi & -ReB1_j \end{bmatrix},$$

$$\boldsymbol{C} = \begin{bmatrix} A2_j & 0 & 0 & 0 \\ 0 & A2_j & 0 & 0 \\ 0 & 0 & A1_j & 0 \\ 0 & 0 & A2_j & -ReA1_J \end{bmatrix}$$

and

$$R_1' = 0,$$

$$R_2' = \left[\frac{-2\,Re}{\Delta T}\left(u_1^n + \frac{2}{Re}\right) - \left(\frac{\partial^2 u_1}{\partial x_1^2} + \frac{\partial^2 u_1}{\partial x_3^2}\right)^n\right] + Re\frac{\partial P^n}{\partial x_1} - 2\,Re(\tfrac{3}{2}H_1^n - \tfrac{1}{2}H_1^{n-1}) - \frac{\partial^2 u_1^n}{\partial x_2^2},$$

$$R_3' = \left[\frac{-2\,Re}{\Delta T}u_2^n - \left(\frac{\partial^2 u_2}{\partial x_1^2} + \frac{\partial^2 u_2}{\partial x_3^2}\right)^n\right] + Re\frac{\partial P^n}{\partial x_2} - 2\,Re(\tfrac{3}{2}H_1^n - \tfrac{1}{2}H_2^{n-1}) - \frac{\partial^2 u_2^n}{\partial x_2^2},$$

$$R_4' = \left[\frac{-2\,Re}{\Delta T}u_3^n - \left(\frac{\partial^2 u_3}{\partial x_1^2} + \frac{\partial^2 u_3}{\partial x_3^2}\right)^n\right] + Re\frac{\partial P^n}{\partial x_3} - 2\,Re(\tfrac{3}{2}H_3^n - \tfrac{1}{2}H_3^{n-1}) - \frac{\partial^2 u_3^n}{\partial x_2^2};$$

also,

$$\phi \equiv \frac{2Re}{\Delta T} + (k_1^2 + k_3^2)_j,$$

$$H_i = -u_l\left(\frac{\partial u_i}{\partial x_l} - \frac{\partial u_l}{\partial x_i}\right) \quad \text{(no summation over } i\text{)}$$

and

$$R_j = \hat{R}_j'.$$

Coefficients of the finite-difference operators that appear in the matrices $\boldsymbol{A}$, $\boldsymbol{B}$ and $\boldsymbol{C}$ are given as

$$C2_j = \frac{2}{\Delta_{j+1}(\Delta_{j+1}+\Delta_j)}, \quad B2_j = \frac{-2}{\Delta_{j+1}\Delta_j}, \quad A2_j = \frac{2}{\Delta_j(\Delta_{j+1}+\Delta_j)},$$

$$C1_j = -A1_j = \frac{1}{\Delta_{j+1}-\Delta_j}, \quad \Delta_{j+1} = (x_2)_{j+1} - (x_2)_j.$$

Since all the flow variables in the solution vector contain an imaginary and a real part, the block-inversion process is applied twice for each pair of k_1 and k_3, which are the wavenumbers along x_1 and x_3 respectively.

The assumption of periodicity in x_1 and x_3 eliminates the necessity of applying explicit boundary conditions along these directions. However, owing to the presence of solid boundaries along the x_2 direction, no-slip boundary conditions are imposed on u_1, u_2 and u_3, and the pressure at the wall is calculated by a second-order approximation from the interior of the flow field. That the pressure boundary conditions are consistent with the x_2 momentum equation at the wall has been shown by Moin *et al.* (1978).

Initial conditions were prescribed from the two- and three-dimensional eigensolutions of the Orr–Sommerfeld equation by considering that, even for subcritical Reynolds numbers, plane channel flow can be driven to instability if the least stable two-dimensional finite-amplitude Orr–Sommerfeld eigenmodes are made to interact with finite-amplitude three-dimensional eigenmodes (Orsag & Kells 1981). The most-explosive situation arises when the three-dimensional eigenmodes are aligned with the main flow direction at $\pm 45°$–$\pm 60°$. Accordingly, we have used the following Benney–Lin-type initial conditions:

$$\boldsymbol{u}(\boldsymbol{x}) = U(x_2, 0, 0) + u_{2\mathrm{D}}(x_2)\, \mathrm{e}^{\mathrm{i}\alpha x_1} + u_{3\mathrm{D}}(x_2)\, \mathrm{e}^{\mathrm{i}\alpha x_1 \pm \mathrm{i}\beta x_3}. \tag{8}$$

Here $U(x_2, 0, 0)$ is the parabolic velocity profile of plane channel flow. The eigenfunctions $u_{2\mathrm{D}}(x_2)$ and $u_{3\mathrm{D}}(x_2)$ correspond respectively to two-dimensional and three-dimensional solutions of the Orr–Sommerfeld equation at $Re = 1500$. The two-dimensional solution was obtained for $\alpha = 1$, whereas the three-dimensional solution was obtained for $\alpha = 1$, $\beta = \pm 1$. A computer program that essentially uses the Kaplan filtering technique was used for the solution of the Orr–Sommerfeld equation (Reynolds 1967). The final amplitudes were chosen so that the maximum value of the x_1 directional two-dimensional disturbance was set equal to $0.11 U_0$, and the maximum amplitudes of the x_1 directional three-dimensional disturbances were each set equal to $0.05 U_0$. Note that recent work by Herbert (1983) has shown an alternative path to transition in plane channel flow via three-dimensional subharmonic instabilities. The existence of a similar mechanism consisting of a resonant triad of Orr–Sommerfeld waves was found by Craik (1971) in boundary layers. However, for large-amplitude disturbances, Herbert (1983) finds evidence for the existence of both Herbert-type (characterized by the formation of a staggered system of Λ-vortices) and Benney–Lin type (characterized by peak–valley splitting) mechanisms during transition depending on initial conditions. The role of subharmonic instability during the final stages of transition is not yet understood, and could very well be the subject of another study. In this work, however, we incorporate the Benney–Lin-type initial conditions, which have been shown to provide a path to transition by previous workers (Orszag & Kells 1980; Orszag & Patera 1981; Kleiser 1982; Wray & Husseini 1984).

3. Results and discussion

The finite-difference system (7) was solved on the CYBER-203 vector processor at NASA/Langley Research Center. A $32 \times 51 \times 32$ mesh was employed along the x_1, x_2 and x_3 directions respectively. The computer code was fully vectorized, and vectorized library subroutines were used for the main computational operations that the solution technique employs. These vector operations are mainly one-dimensional fast Fourier transforms (FFT) to calculate spatial derivatives with the pseudospectral method, two-dimensional FFT to transform the equations into (k_1, k_3) wavenumber space, and block-tridiagonal matrix inversion along x_2. For the FFT operations typical vector lengths were around 1000, which is an optimal vector length to take full advantage of the vector processor. For the block-tridiagonal matrix inversion (which essentially is a scalar operation), a vectorized subroutine that inverts a large number of tridiagonal systems simultaneously was used. This procedure decreases CPU time significantly by reducing the number of scalar operations required to invert each system separately. The fully vectorized code takes about 10 s of CPU time per time step for the $32 \times 51 \times 32$ mesh to solve the finite-difference system (7) on a

computational box in which the flow is confined between rigid walls at $x_2 = \pm 1$. Periodicity lengths (box lengths) along x_1 and x_3 were chosen so that the smallest wavenumbers allowed in the computational domain were equal to $\alpha = 1$ and $\beta = 1$ respectively, i.e. the box length was set equal to 2π along these directions.

It should be recalled that the time-advancing scheme employed in this work is partly explicit (on the convective terms) and partly implicit (on the diffusion and pressure terms). Although in view of linear stability analysis implicit methods are unconditionally stable (extrapolation to nonlinear equations is sometimes vague), the mixed nature of the present scheme as well as the time-accurate nature of the problem under investigation necessitate adherence to stability bounds of explicit schemes. Therefore, in all the calculations reported herein, the convective stability condition (the Courant–Friedrichs–Lewy condition), which requires the Courant number $\mathscr{C}$ to be always less than one, and the diffusive stability condition were obeyed. With $(\Delta x_2)_{\min} = 0.0092$ and $\Delta T = 0.025$, where ΔT is the non-dimensional time step, through the course of the calculations $\mathscr{C}$ varied as

$$\mathscr{C} \equiv \Delta T\left(\left|\frac{u_1}{\Delta x_1}\right| + \left|\frac{u_2}{\Delta x_2}\right| + \left|\frac{u_3}{\Delta x_3}\right|\right)_{\max} \leqslant 0.2, \tag{9}$$

whereas the diffusive stability criterion D was equal to

$$D \equiv \frac{1}{Re}\left[\frac{\Delta T}{(\Delta x_2)^2_{\min}}\right] \leqslant 0.04, \tag{10}$$

so that the diffusive stability condition, which requires $D < 0.5$, was also always satisfied. The computer program was tested by calculating the growth rates of small-amplitude Orr–Sommerfeld waves. For a wide range of Reynolds numbers (between 1000 and 10000), the agreement between the computed results and the linear theory was better than 0.5%. As a further test on the solution accuracy, calculations were reperformed after halving the time step at various intervals during the computation. For the values of $\mathscr{C}$ and D as given above, the difference between such calculations was negligible.

In the subsequent parts of this section, results obtained from the numerical integration of the finite-difference system (7) for the time evolution of the initial disturbances are compared with the experiments of Nishioka *et al.* (1981). It should be noted that there are several differences existing between the conditions of the experiment and the present computations. First, the periodic boundary conditions employed in the computations along x_1 and x_3 are not realized in the laboratory, where the flow is periodic in time. Secondly, because of periodicity, the computational flow evolves in time, not in space–time as in the laboratory. One justification to the first difference can be advanced on the basis of previous numerical experiments: transition simulations of the flat-plate boundary layer (Orszag 1976) and of the plane channel flow (Fasel *et al.* 1977) with proper inflow–outflow boundary conditions gave similar results to those simulations in which periodic boundary conditions were used. Furthermore, Wray & Hussaini (1984) showed that their periodic boundary-layer simulations compared very favourably with the experiments of Kovasznay *et al.* (1962), demonstrating the absence of any important adverse effects of the artificial boundary conditions they employed. In a recent survey article, Herbert (1981) also stresses these similarities and advocates a more tolerant attitude towards the differences existing between time and space–time evolution. We share the opinion of these workers and expect the periodic boundary conditions of the present computations not to introduce any significant drawbacks for comparisons with the laboratory

flow. The assumption of streamwise periodicity, which implies the evolution of the flow in time, enables the most efficient use of available computer resolution by resolving only one wavelength. This assumption can be justified on the grounds that, in a coordinate frame moving with the phase velocity of the two-dimensional disturbance field, the spatial evolution of the laboratory flow is essentially equivalent to temporal growth. A third difference between the experiment and the computation is the Reynolds number. The laboratory flow has a subcritical Reynolds number $Re = 5000$, whereas the computation was done at a lower subcritical Reynolds number $Re = 1500$. The selection of a higher Reynolds number (e.g. in the linearly unstable range) makes the governing equations very stiff and requires the use of extremely small time steps for numerical stability. Hence the selection of $Re = 1500$ was mainly to force the computation into transition and breakdown with the least amount of computer expense. It should be noted that wall phenomena characteristic of the final stages of transition are essentially independent of Reynolds number, as observed by Nishioka *et al.* (1981) for channel flow and by Smith & Metzler (1982) for boundary-layer transition. Therefore the difference between the Reynolds numbers of the experiment and the simulation should not have any important consequences for the qualitative comparisons between the two sets of results.

In their experiments, Nishioka *et al.* (1981) identified the various stages of transition according to the number of spikes appearing in the oscilloscope traces of the disturbance velocity u_1'. Since the time axis of the experiment is interchangeable with the x_1 axis of the computation, we obtain similar traces by plotting u_1' along x_1 (over two periods) as shown in figure 1. In this figure the first frame shows the sinusoidal variation of the initial conditions at $T = 0$. This is followed by the nonlinear distortions of the initial conditions, resulting in variations of u_1' which strongly resemble the oscilloscope traces at the one-, three- and five-spike stages of the laboratory flow. In particular, the variations of u_1' with x_1 at $T = 44$ are very similar to the ensemble-averaged waveforms presented by Nishioka *et al.* at the five-spike stage. The last frame in figure 1 shows variations of u_1' at a time ($T = 79$) much later than the occurrence of the five-spike stage ($T = 44$). Here we note the absence of fluctuations of rich frequency content that are characteristic of fully developed turbulence; this lends support to the idea that the last stage of transition may not be as spontaneous and explosive a phenomenon as generally supposed. However, at this stage, the u_1' variations are very similar to velocity oscillations observed in wave packets and indicate the occurrence of 'patches' of turbulent fluid. For the remainder of this discussion, results from the simulation at the spike stages (shown in figure 1) will be used, whenever possible, for comparisons with the corresponding spike stages of experiments of Nishioka *et al.* We have found this to be the more appropriate means of matching instantaneous events because of the difficulty in establishing appropriate length- and timescales in the laboratory flow. Note that the experiment is performed in such a way that the wave growth in the streamwise direction x_1 is simulated at a *fixed* x_1 position by varying the amplitude of the initial disturbances.

In figure 2 we show a history of the time evolution of the flow in terms of the maximum amplitude of the two-dimensional primary disturbance, its two-dimensional harmonic and the three-dimensional primary disturbance. The trends displayed by these quantities are generally similar to the results of Orszag & Kells (1980), which they obtained from computations performed at $Re = 1250$. The main features of these trends are the rapid decrease in the two-dimensional primary-wave amplitude and the rapid increase of the amplitude of its harmonic. Also, the three-dimensional

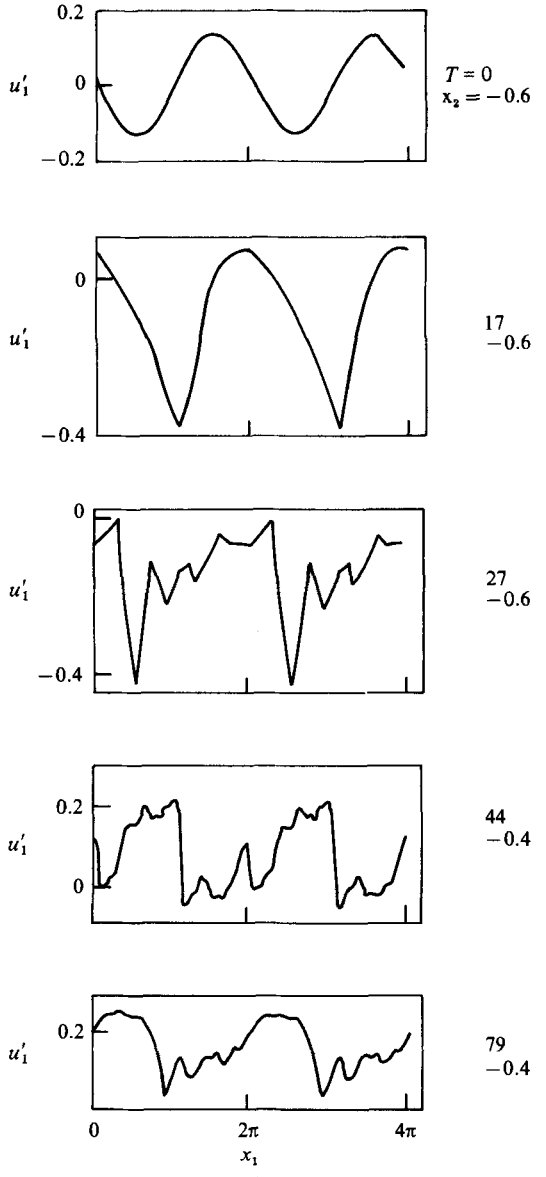

FIGURE 1. Development of u_1' fluctuation in time along x_1.

primary-wave amplitude first increases, then gradually decreases at around $T = 30$. In the present calculations we observe that variations of the amplitudes start to fluctuate as early as $T = 15$, but, even at later times, the fluctuations do not display an explosive trend. That no 'explosive' instabilities were found in the present computations is in accord with the findings of Nishioka *et al.* (1980), which imply that breakdown in channel flow is as gradual as the growth of instabilities found in free shear flows.

In figure 3 we present plots of maximum root-mean-square (r.m.s.) amplitudes of u_1, $(u_{1\,\mathrm{rms}})_{\max}$, over two periods along x_3. Here we define the r.m.s. value as an average over x_1. We note that at $T = 0$ the wave pattern is sinusoidal and corresponds to peaks at $x_3 = 0$, 2π, 4π and to valleys at $x_3 = \pi$, 3π. Subsequently, at later times

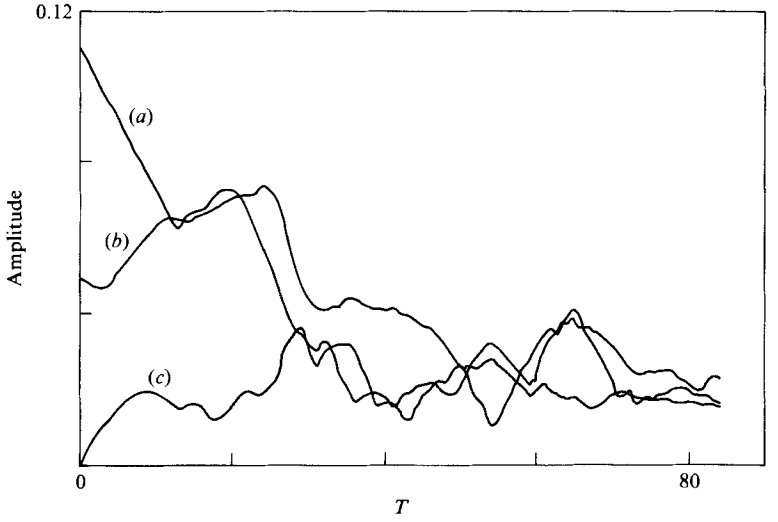

FIGURE 2. Time history of maximum disturbance amplitudes: (*a*) two-dimensional primary; (*b*) three-dimensional primary; (*c*) two-dimensional harmonic.

the nonlinear distortions of the wavefront result in minima occurring at the peaks and maxima occurring at the valleys in accordance with the experiments of Nishioka *et al.* (1980). At later times, an increase in the frequency of the peak–valley structure is clearly evident, suggesting an increase in the number of characteristic vortex structures along x_3.

Plots of velocity profiles averaged over the (x_1, x_3)-plane, $\langle u_1 \rangle$, are shown in figure 4 for laminar (initial), late transition and 'early-turbulence' stages at $T = 0$, 44 and 79 respectively. The $\langle u_1 \rangle$ distribution at $T = 79$ has a strong resemblance to the turbulent channel-flow profile, with increased velocity gradient at the wall and with a full profile indicative of turbulent mixing. Note that, owing to the averaging process, the $\langle u_1 \rangle$ distributions do not exhibit any inflexions. However, the characteristic inflexional profiles are depicted in the distributions of the instantaneous velocity profiles (figure 5). As noted by Orszag & Kells (1980), the occurrence of such fluctuations (inflexions) close to the wall indicates that the nonlinear interaction of two- and three-dimensional waves close to the wall is the fundamental mechanism that drives the flow to instability. This is in accord with the idea that the flow will be receptive only to a selected band of spanwise wavenumbers, the most 'dangerous' of which result in three-dimensional disturbances with maxima occurring close to the walls. In figure 6 the velocity profile $\langle u^+ \rangle = \langle u_1 \rangle / u_\tau$ versus $y^+ = x_2 u_\tau / \nu$ is plotted; here u_τ is the friction velocity and is calculated from $\mathrm{d}\langle u_1 \rangle / \mathrm{d}x_2$ at the wall times $1/Re$. At $T = 17$ the profile follows the laminar relation $u^+ = y^+$, and the change from $T = 17$ to $T = 79$ shows a gradual approach to the law of the wall. At $T = 44$ the Reynolds number based on the friction velocity is equal to 69 and, as expected, is larger than its initial (laminar) value of 55.

Plots of plane-averaged fluctuation intensities $\langle (u_1 - \langle u_1 \rangle)^2 \rangle$ are shown in figure 7 at various T. There are several interesting features of this figure. First, at $T = 17$, the shift in the position of peak amplitude towards the channel centre ($x_2 = -0.6$), as well as the increase in the maximum amplitude, indicate that the development of the computed flow field is compatible with experimental observations pertaining to the one-spike stage of the transition process (Tani 1969). It will later be shown

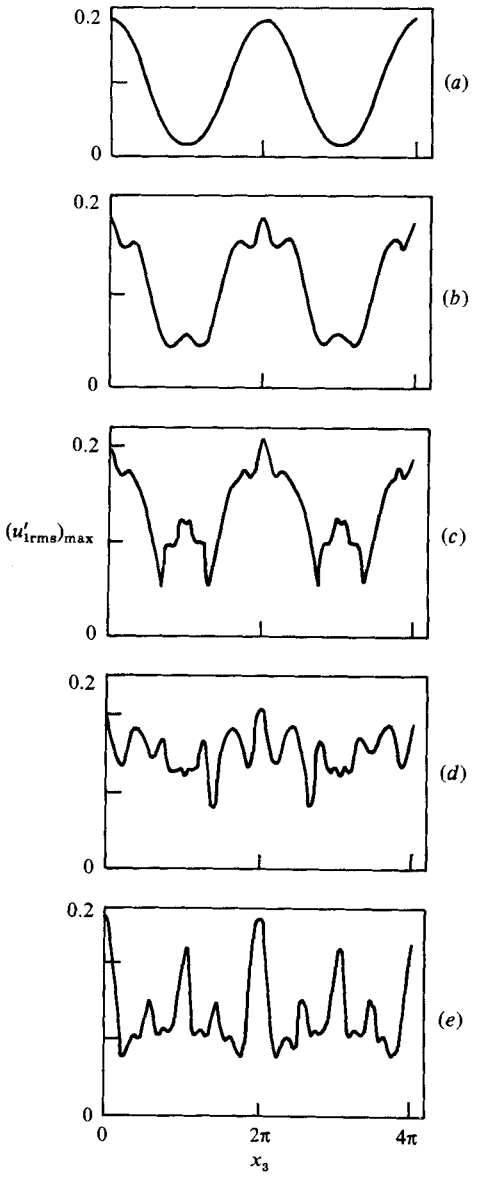

FIGURE 3. Development of the peak–valley structure in terms of maximum $(u_1')_{\text{rms}}$: (*a*) $T = 0$; (*b*) 17; (*c*) 27; (*d*) 44; (*e*) 79.

that during this stage there is a substantial increase in the spanwise vorticity ω_z away from the lower wall around $x_2 = -0.6$. Secondly, in accordance with the laboratory flow of Nishioka *et al.* (1981) at later stages, the computed intensity profile displays a second peak occurring close to the wall associated with turbulence production. At $T = 44$, corresponding to the five-spike stage, we see that peak intensity has reached a value typical of turbulent channel flow; however, the peak occurs uncharacteristically away from the wall. Finally, at $T = 79$, the peak in the intensity profile has moved towards the wall, but even at this stage the distribution has not assumed the asymptotic fully turbulent form. In figure 8 plots of plane-averaged shear-stress $\langle (u_1 - \langle u_1 \rangle) u_2 \rangle$ profiles are shown. The increase in the magnitude of the shear stress

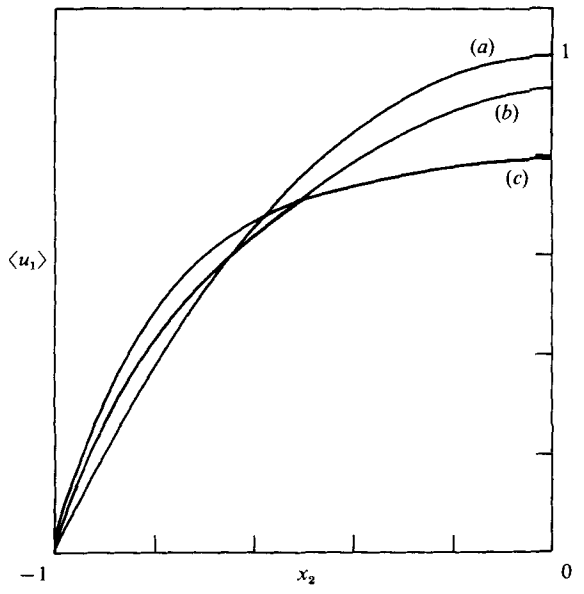

FIGURE 4. Plots of plane-averaged mean-velocity profiles: (*a*) $T = 0$; (*b*) 44; (*c*) 79.

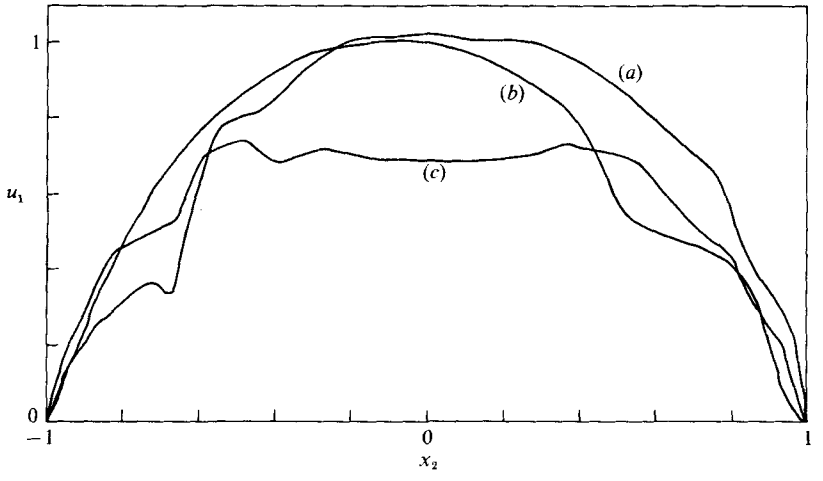

FIGURE 5. Plots of instantaneous velocity profiles at $x_1 = \frac{3}{2}\pi$, $x_3 = \frac{1}{2}\pi$: (*a*) $T = 17$; (*b*) 44; (*c*) 79.

from $T = 0$ to $T = 17$ clearly indicates the effects of nonlinearity in transferring energy from the mean flow to the fluctuating motion. At the five-spike stage ($T = 44$) the maximum shear stress has attained a value typical of turbulent channel flow. However, the location of the maximum is away from the wall, and roughly corresponds to the location of the peak in the respective intensity profile (figure 7). It can thus be inferred that, at this stage of the computation, the energy-exchange mechanism of fully developed wall turbulence is not yet reflected by the plane-averaged velocity correlations.

Spanwise variations of u_1 are plotted at various distances along x_2 in figures 9(*a–e*). In figure 9(*a*) we show the initial distributions, which are highly three-dimensional. At $T = 17$ (figure 9*b*) the distributions indicate a velocity defect both at peak and

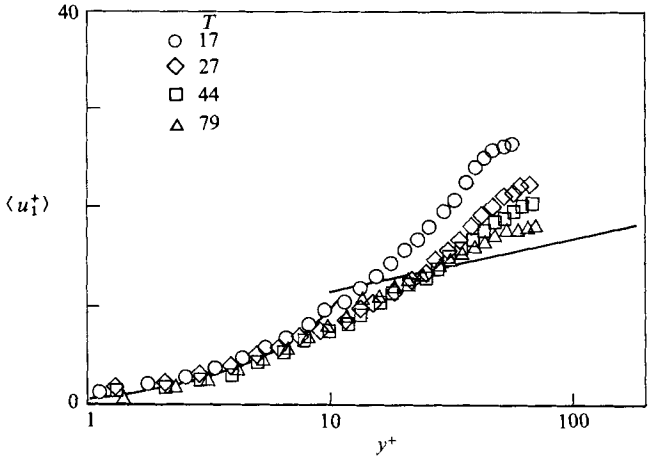

FIGURE 6. Plots of plane-averaged mean velocity in wall units.

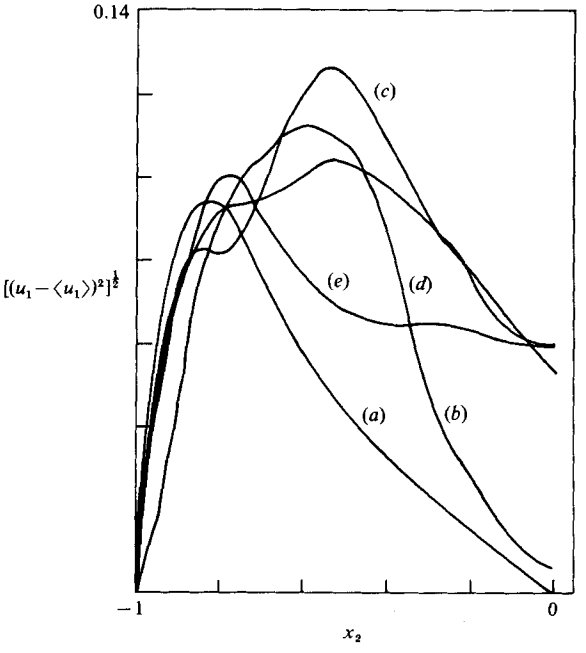

FIGURE 7. Plots of plane-averaged fluctuation intensities of u_1: (*a*) $T = 0$; (*b*) 17; (*c*) 27; (*d*) 44; (*e*) 79.

at valley as well as a velocity excess in between. This is indicative of intensification of the initial streamwise vortices and appearance of weaker streamwise vortex pairs in accordance with the Benney–Lin (1960) theory. Subsequently, figures 9(*c–e*) display the formation of additional vortex pairs, indicating transport of energy down the wavenumber spectrum. The spanwise symmetry imposed by the initial conditions is retained through the five-spike stage. At this stage, an estimate of the flow-field resolution can be obtained from the spanwise distance λ_z between peak positions. Non-dimensionalized by u_τ and ν, typically $\lambda_z = 115$. This is larger than but comparable to $\lambda = 80$, which is the typical spanwise length in the laboratory flow

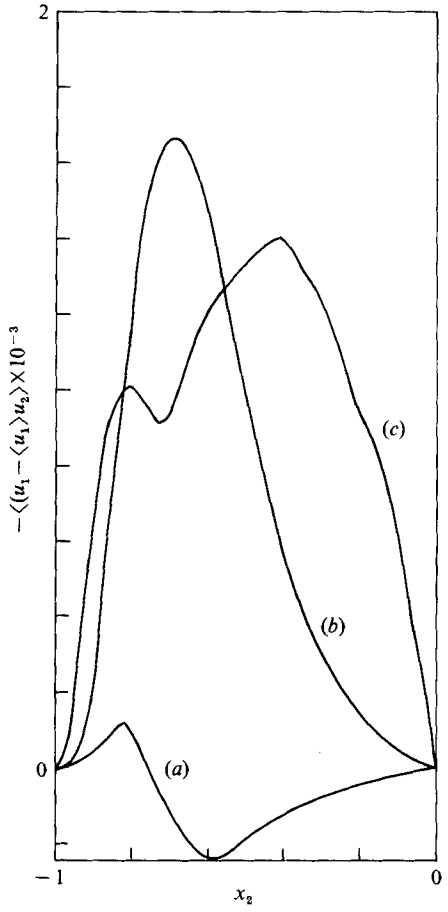

FIGURE 8. Plots of plane-averaged shear stress: (*a*) $T = 0$; (*b*) 17; (*c*) 44.

during the five-spike stage (Nishioka *et al.* 1981). It should be noted that the spanwise characteristic length in wall turbulence is about 100. Therefore it could be asserted that at this stage the present results are representative of *initial* wall turbulence.

A more detailed description of the transition process can be obtained from contour plots of equishear lines $\partial u_1/\partial x_2$ (which correspond to approximate spanwise vorticity ω_z) in the (x_1, x_2)-plane at the position of maximum u_1/U_0. Results from the computation that correspond to the various stages of the laboratory flow are presented in figures 10–15 between the lower wall ($x_2 = -1.0$) and the channel centre ($x_2 = 0$). In figures 11(*a*)–13(*a*), figures 4–6 of Nishioka *et al.* (1981) are also shown for a qualitative comparison with the present results. In figure 10 contour plots corresponding to the initial conditions and in figure 11 contour plots corresponding to the 'one-spike' stage ($T = 0$ and $T = 17$ respectively) are shown. In both the laboratory flow and the computation, the typical head of the shear layer appears very clearly at the one-spike stage, indicating the formation of a shear layer away from the wall at about $x_2 = -0.6$ due to the induced velocity from the streamwise vortex system. In addition, the sudden dip of the shear layer from the high-velocity outer flow to the low-velocity region clearly appears as a kink in both the computation and the laboratory flow. Since the grid points are finely clustered along x_2 close to the

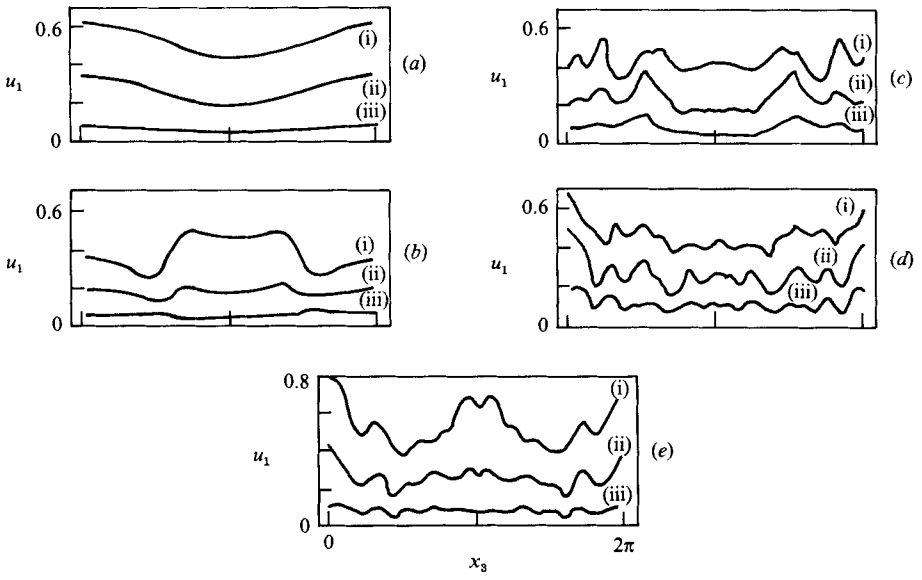

FIGURE 9. Spanwise variations of u_1 at x_1 corresponding to $(u_1)_{max}$: (*a*) $T = 0$; (*b*) 17; (*c*) 27; (*d*) 44; (*e*) 79. In each part: (i) $x_2 = -0.968$; (ii) -0.903; (iii) $x_2 = -0.764$.

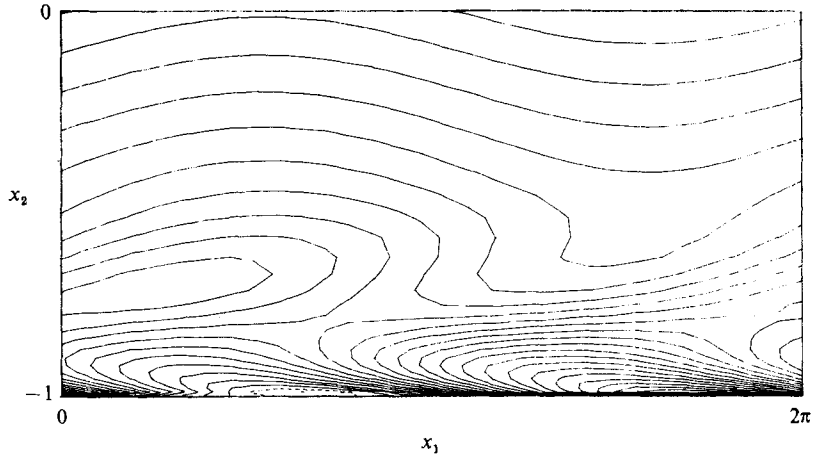

FIGURE 10. Contour plots of $\partial u_1/\partial x_2$ at $T = 0$ in the (x_1, x_2)-plane; contours from -4.0–4.2. Flow direction is from left to right.

wall, vorticity concentrations in this region are also adequately resolved by the numerical simulation.

Figure 12 shows equishear lines at $T = 27$, corresponding to the three-spike stage of the laboratory flow. Owing to the secondary instability manifested in the previous stage, breakdown of flow structures into smaller scales is observed in both the experiment and the computation. The growth of the kinked portions of the equishear lines into the so-called 'hairpin eddies' is clearly depicted in the experiment. The computation displays a similar evolution: the head of the shear layer is lifted up towards the channel centreline, and the kink in the shear layer is quite apparent in this stage of the simulation. Simultaneously, with this activity taking place in the

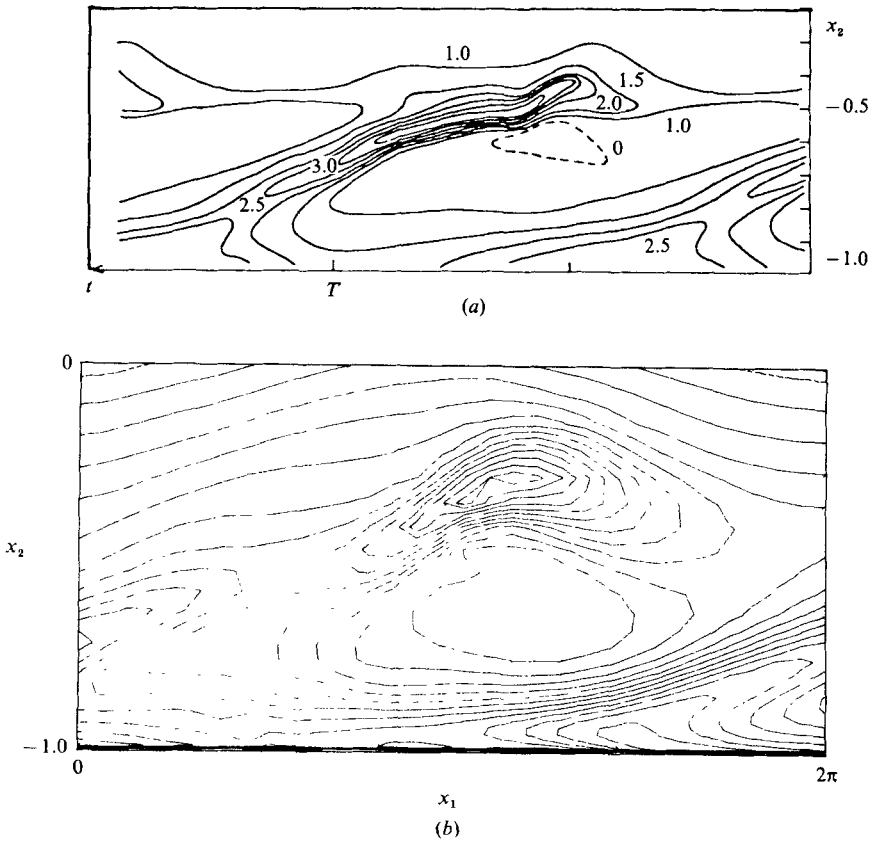

FIGURE 11. Contour plots of $\partial u_1/\partial x_2$: (*a*) One-spike stage, figure 4 from Nishioka *et al.* (1981); (*b*) computations at $T = 17$ in the (x_1, x_2)-plane, contours from −0.2–2.6. Flow direction is from left to right.

outer (high-speed) portions of the flow field, both the experiment and the computation show an intense shear layer developing close to the wall, which is indicative of turbulence generation. It is generally agreed that hairpin eddies that are lifted towards the centreline erupt into turbulent spots. However, figure 12 indicates that wall turbulence may also be closely associated with vorticity dynamics simultaneously taking place with the eruption of hairpin eddies. Contours of equishear lines at $T = 44$, corresponding to the five-spike stage of the experiment, are shown in figure 13. In both the experiment and the computation, the intense shear layer developed in the wall region is clearly discernible. It should also be noted that the spanwise position of maximum ω_z appears very close to the wall and does not necessarily coincide with the spanwise location of maximum u_1/U_0 where the contours are presented. The most significant feature of figure 13 is the existence of distinct vortex structures in the wall region in both the laboratory flow and the computation. These vortices are inclined to the main flow direction at an angle that varies between approximately 14°–40° and show a close resemblance to the energetic horseshoe vortices characteristic of initial wall turbulence (Hama & Nutant 1963; Klebanoff *et al.* 1962). It is these vortices roughly aligned along the direction of maximum extensional stress that are mainly responsible for extracting energy from the mean shear (Tennekes & Lumley 1972).

In figure 14 equishear lines at spanwise locations $x_3 = (x_3)_0 + 2\Delta x_3$ and

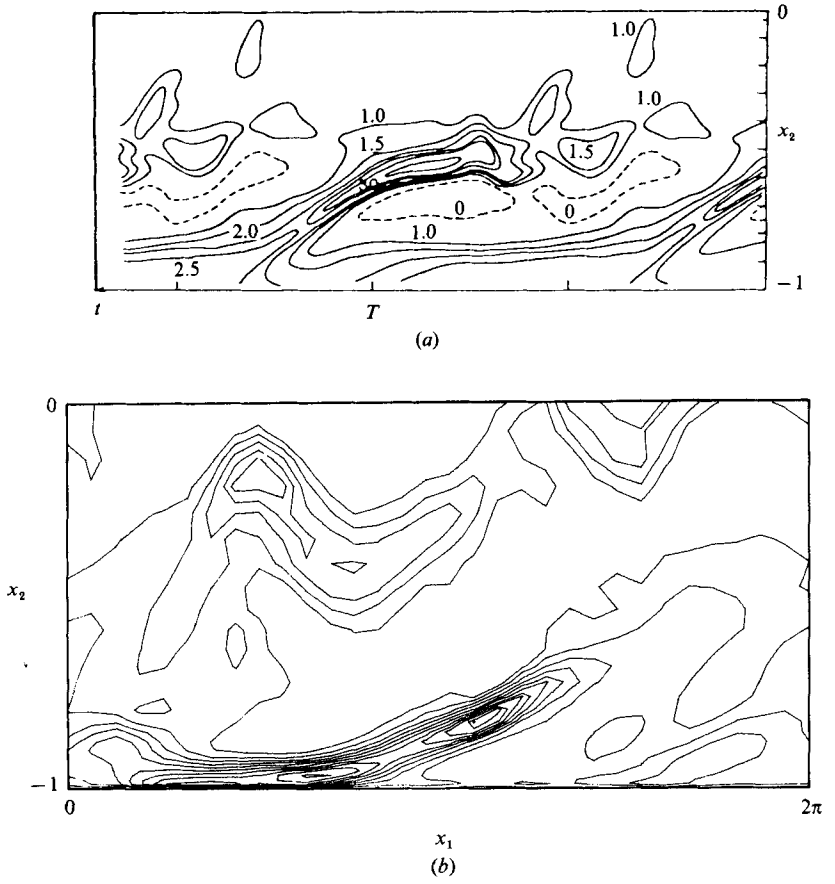

FIGURE 12. Contour plots of $\partial u_1/\partial x_2$: (*a*) three-spike stage, figure 5 from Nishioka *et al.* (1981); (*b*) computations at $T = 27$ in the (x_1, x_2)-plane, contours from 0.3–6.8. Flow direction is from left to right.

$x_3 = (x_3)_0 + 4\,\Delta x_3$ at $T = 44$ are compared. Here we define $(x_3)_0$ as the spanwise position corresponding to figure 13, and Δx_3 is the mesh size along x_3. Figure 14 suggests that the shear layer is formed from a system of horseshoe vortices in succession such that, as the first-born vortex erupts into the channel centre, a new one forms at the wall. As evidenced in figure 5, the vortex lift-up is still clearly discernible at the 'early-turbulence' stage $T = 79$. Here we note the vortex lift-up towards the channel centre, but its extension is considerably shorter than that observed previously at the five-spike stage. This variance suggests the existence of different vortex structures characteristic of these two stages. In fact, we shall show later that the typical horsehoe vortex of late transition is not the basic structure of early turbulence.

The above comparisons reveal a close similarity between the present results and the experiments of Nishioka *et al.* (1981), lending justification to the use of the time-evolving computed flow field as a supplement to the space–time-evolving laboratory flow. As a step in this direction, we now examine the behaviour of various flow-field quantities that were not measured in the experiment. In figures 16–20 we show contours of ω_x (streamwise vorticity) and ω_z (spanwise vorticity) at various instances in time. The contours in the (x_1, x_3)-plane are at $x_2 = -0.99$, corresponding

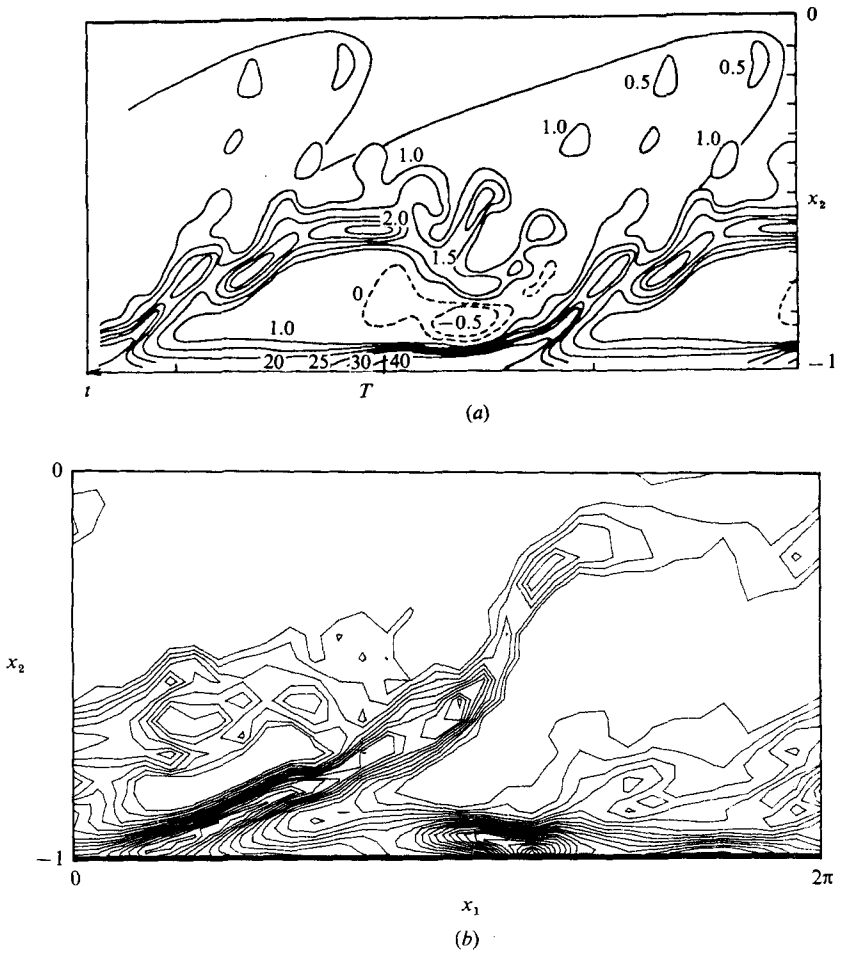

FIGURE 13. Contour plots of $\partial u_1/\partial x_2$: (*a*) five-spike stage, figure 6 from Nishioka *et al.* (1981); (*b*) computations at $T = 44$ in the (x_1, x_2)-plane, contours from 0.7–7.0. At this spanwise position we define $x_3 \equiv (x_3)_0$. Flow direction is from left to right.

to the first computational point away from the lower wall. Figure 16 displays the counter-rotating vortex pairs due to the prescribed initial conditions with strength considerably weaker than the initial spanwise vorticity. Figure 17 (*a*) shows contours of ω_x at $T = 17$, corresponding to the one-spike stage. At this stage the initial counter-rotating vortex pairs are still evident. Also apparent is the significant amount of vorticity production by stretching of ω_x at an angle of about 30° to the x_1 direction, roughly corresponding to maximum extensional stress in the (x_1, x_3)-plane. Note that vorticity dynamics is governed by the vorticity-transport equation, which reads (Tennekes & Lumley 1972)

$$\frac{\partial \omega_i}{\partial t} + u_j \frac{\partial \omega_i}{\partial x_j} = \omega_j \frac{\partial u_i}{\partial x_j} + \frac{\partial^2 \omega_i}{\partial x_j \partial x_j}. \tag{11}$$

In this equation the first term on the right represents stretching (production) of vorticity by the instantaneous shear. In the (x_1, x_3)-plane the dominant shear term is $\partial u_1/\partial x_3$, and the major contribution to the production of ω_x is supplied by

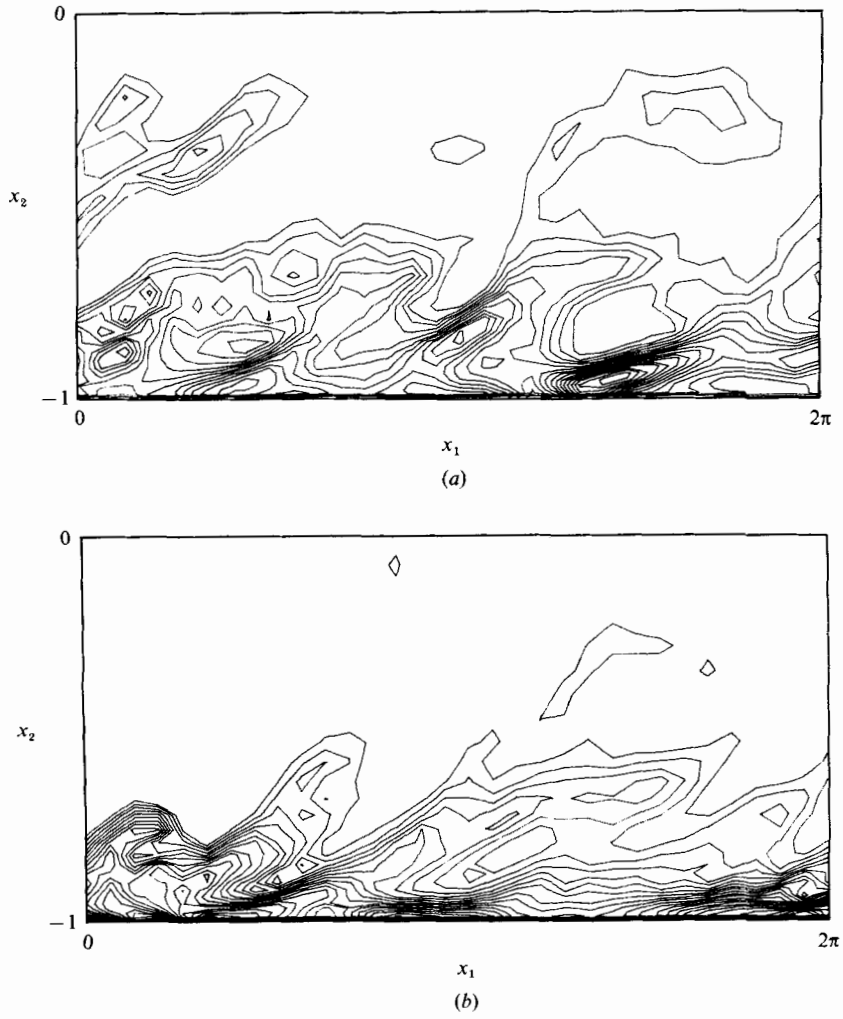

FIGURE 14. Contour plots of $\partial u_1/\partial x_2$ in the (x_1, x_2)-plane at $T = 44$; (*a*) $x_3 = (x_3)_0 + 2\Delta x_3$; (*b*) $x_3 = (x_3)_0 + 4\Delta x_3$. Here Δx_3 is the mesh size along x_3. Flow direction is from left to right.

the stretching term $\omega_3 \partial u_1/\partial x_3$; this is clearly in accordance with figure 17(*a*). In figure 17(*b*) ω_z contours are shown in the same x_2 plane as in figure 17(*a*). Here the formation of Λ-shaped vortices at the peaks corresponding to $x_3 = 0$ and $x_3 = 2\pi$ are clearly depicted. According to Hama & Nutant (1963), the formation of a Λ-shaped vortex comprises the intermediate step during the evolution of the nonlinear distortions of spanwise vorticity into a horseshoe vortex. An intriguing possibility is now suggested by a comparison of figures 17(*a*) and (*b*): the strong correspondence between the spanwise positions of high concentrations of ω_x and ω_z makes it plausible to interpret ω_x as the 'footprints' of the Λ-shaped vortices, not unlike the structures suggested by Perry *et al.* (1981). In figures 17(*c*, *d*) contours of ω_x in the (x_2, x_3) plane at the position of maximum u_1/U_0 are shown at $T = 0$ and $T = 17$ respectively. In accordance with the Benney–Lin (1960) theory, figure 17(*d*) shows the inital system of counter-rotating vortices doubling their frequency. The increase in the magnitude of ω_x is also apparent in this figure.

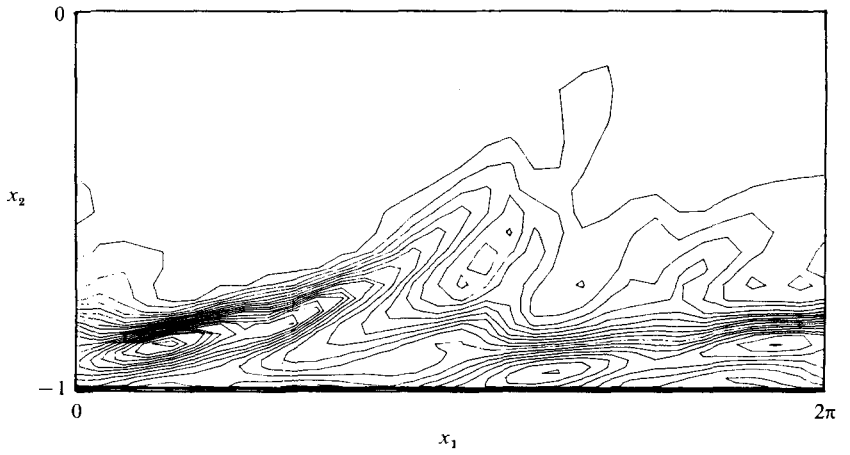

FIGURE 15. Contour plots of $\partial u_1/\partial x_2$ in the (x_1, x_2)-plane at $T = 79$. Contours from 0.26–6.25. Flow direction is from left to right.

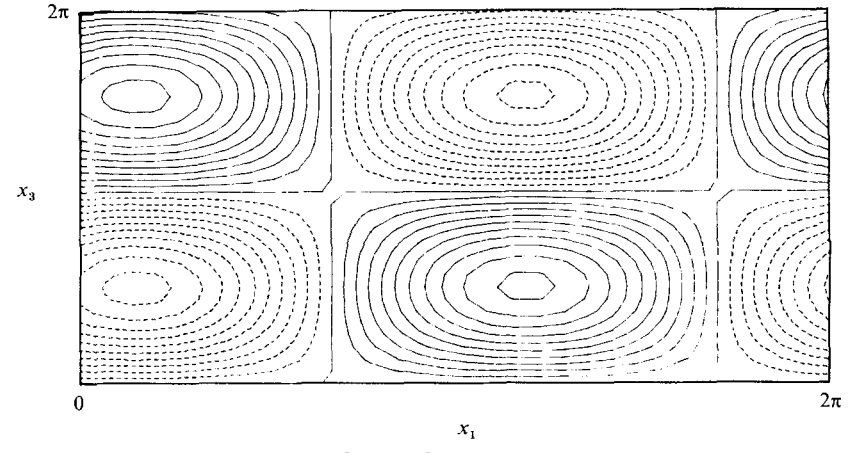

FIGURE 16. Contour plots of ω_x in the (x_1, x_3)-plane at $T = 0$. Contours from -0.2×10^{-2}–0.2×10^{-2}. Flow direction is from left to right.

In figures 18(*a*, *b*) contour plots of ω_x and ω_z are presented at the three-spike stage in the (x_1, x_3)-plane, at $x_2 = -0.991$. Figure 18(*a*) displays the initial vortex pair still stretched at an angle of about 30° to the x_1 axis. Also shown in this figure are newly formed vortex pairs that have decreased lengthscales and that are aligned with the x_1 axis. The alignment of vortex pairs with x_1 (rather than the direction of maximum extensional stress indicating vorticity production) suggests that ω_x has attained a value high enough to enhance the effects of viscous dissipation. This may appear implausible at first, since the frequency spectrum of the velocity field is not yet fully developed; consequently, the dissipation rate of fluctuation energy is slow. But if we note that the spectrum of vorticity (defined in terms of velocity gradients) has a much steeper gradient than the spectrum of the velocity, and consequently vorticity dissipation is shifted to lower frequencies, then at this stage the action of viscous dissipation can be expected to be more pronounced and detectable on vorticity than on the velocity field. Figures 18(*a*, *b*) also show that the spanwise positions of ω_x and

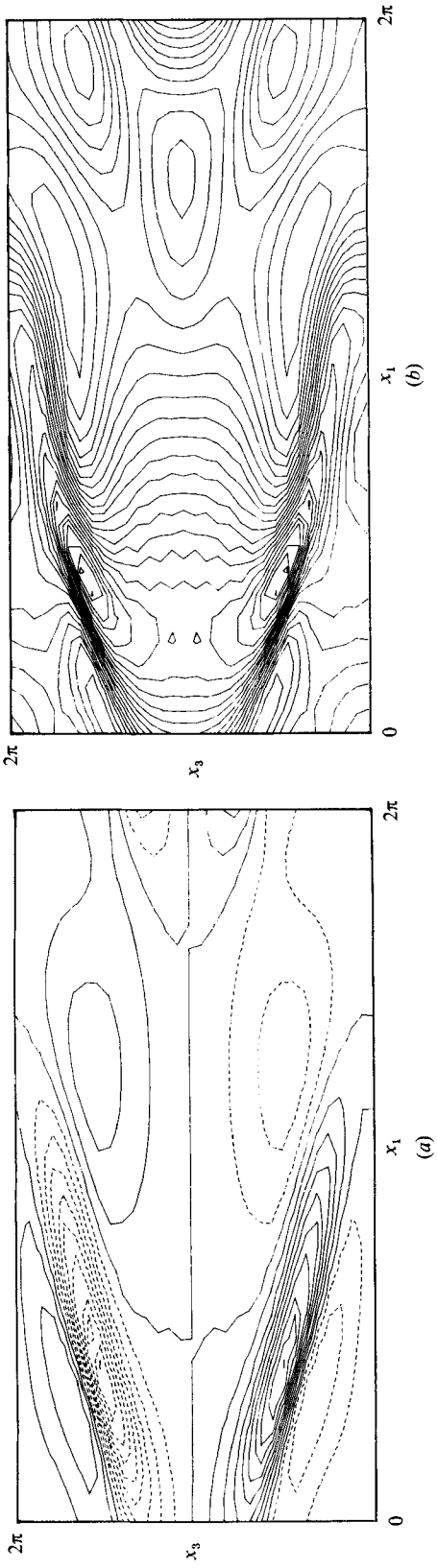

FIGURE 17. Vorticity contours: (*a*) ω_x in the (x_1, x_3)-plane at $T = 17$, contours from -4.5–4.5; (*b*) ω_z in the (x_1, x_3)-plane at $T = 17$, contours from 0.6–2.8; (*c*) ω_x in the (x_2, x_3)-plane at $T = 0$, contours from -0.4×10^{-1} to 0.4×10^{-1}; (*d*) ω_x in the (x_2, x_3)-plane at $T = 17$, contours from -1.0–1.0. In (*a*) and (*b*) flow direction is from left to right, and in (*c*) and (*d*) flow direction is into the (x_2, x_3)-plane.

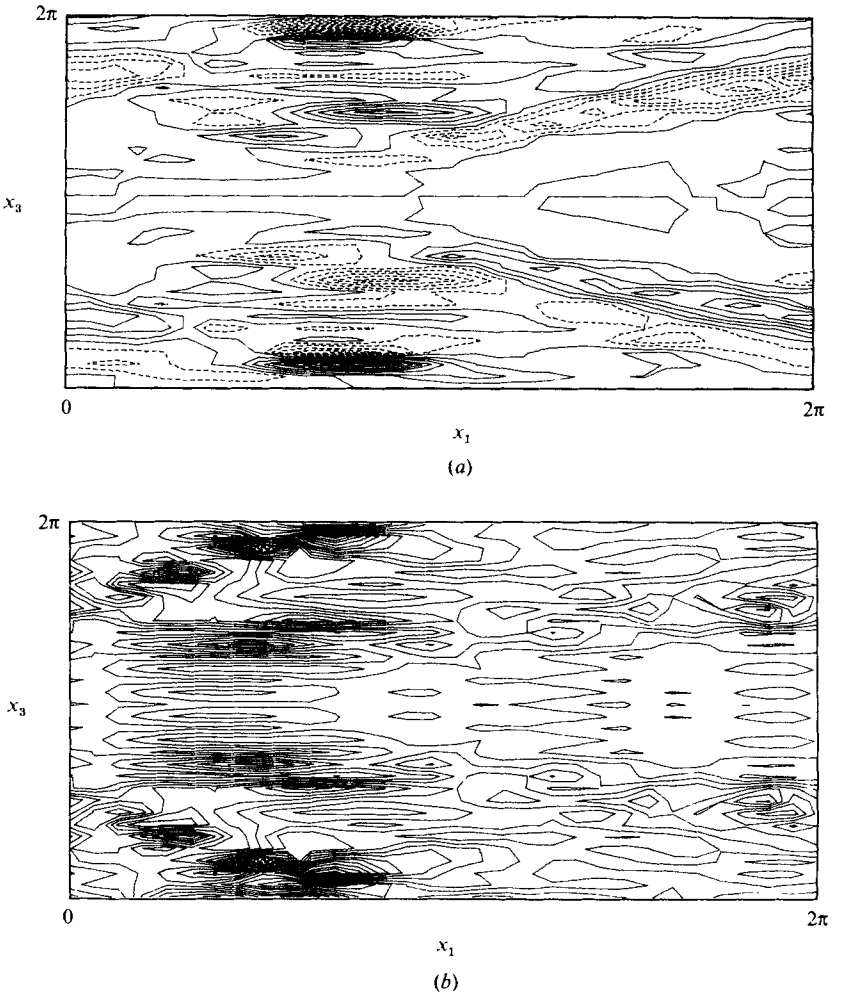

FIGURE 18. Vorticity contours in the (x_1, x_3)-plane at $T = 27$; (*a*) ω_x, contours from -7.2–7.2; (*b*) ω_z, contours from -1.0 to 7.5. Note that high concentrations of ω_x and ω_z appear at roughly the same position. Flow direction is from left to right.

ω_z concentrations are almost juxtaposed as observed previously in figures 17(*a*, *b*), supporting the idea that ω_x can be interpreted as the footprints of the vortex loop. As inferred from these figures, the characteristic dimension of the Λ-shaped vortices at the peaks corresponding to $x_3 = 0$ and $x_3 = 2\pi$ are reduced along both x_1 and x_3. This is most likely due to the formation of horsehoe vortices that are narrower along x_3 and are elevated with respect to the (x_1, x_2)-plane; similar trends are displayed in figures 19(*a*, *b*) at $T = 44$, corresponding to the five-spike stage. In figure 20 details of ω_x contours in the vicinity of the lower wall are shown in the region between the lower wall ($x_2 = -1.0$) and $x_2 = -0.92$. Here the most interesting aspect is the existence of distinct patterns of alternating pairs of positive and negative vorticity. Note that high concentrations of streamwise vorticity in this figure exist at the same x_3 location as in figure 19. As explained above, alternating pairs of streamwise vorticity are associated with the induced velocity field responsible for the distortion and production of spanwise vorticity, and seem to form the extensions of

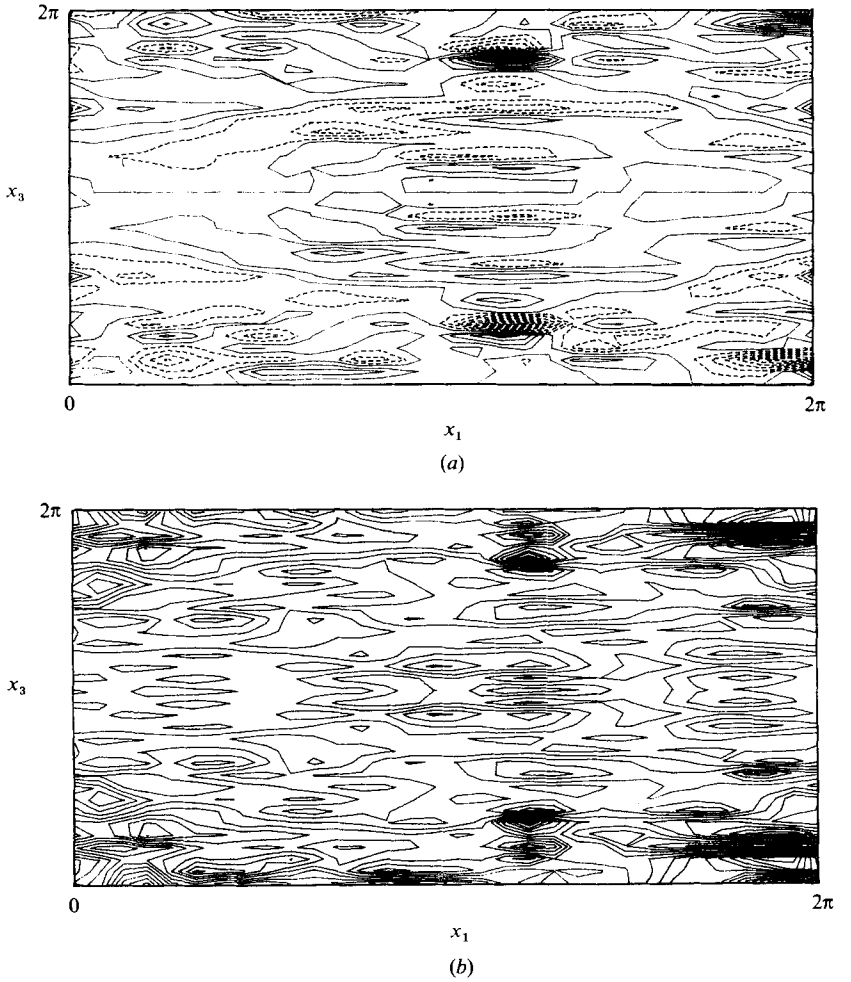

FIGURE 19. Vorticity contours in the (x_1, x_3)-plane at $T = 44$: (*a*) ω_x, contours from -5.6–56; (*b*) ω_z, contours from 0 to 8.5. Flow direction is from left to right.

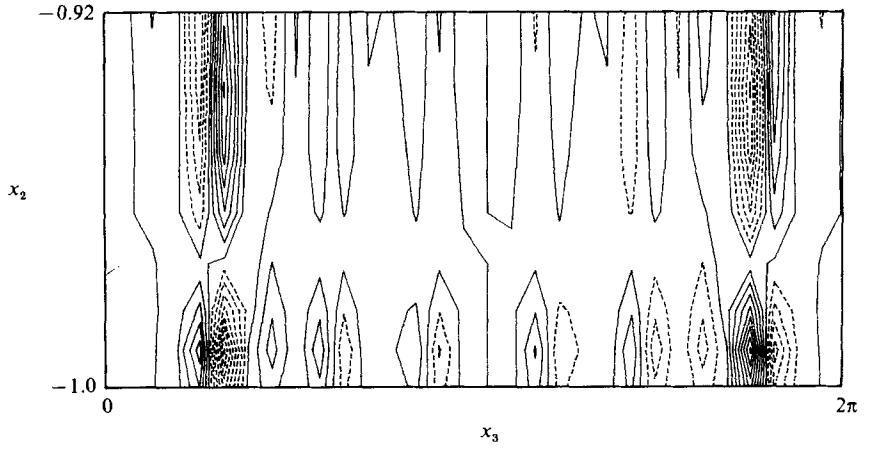

FIGURE 20. Contour plots of ω_x in the (x_2, x_3)-plane in the vicinity of the lower wall at $T = 44$. Contours from -5.6–5.6. Flow direction is into the (x_2, x_3)-plane.

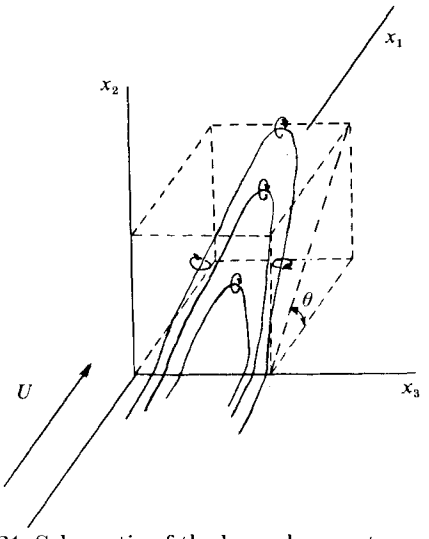

FIGURE 21. Schematic of the horseshoe-vortex system. The angle θ typically varies between 14° and 40°.

the horsehoe vortices. The pressure field associated with this vortex system is discussed by Biringen & Maestrello (1984), indicating flow-field structures evolving in a manner consistent with the observations of Carlson, Widnall & Peeters (1982) in their flow-visualization experiments. Based on these observations, it now seems plausible to suggest that the main element of the nonlinear transition process during the final stage is a system of horseshoe vortices with extensions or 'footprints' in the (x_1, x_3)-plane. A schematic of this system of vortices is given in figure 21. This concept is similar to the structures inferred by Head & Banyopadhyay (1981) from flow visualization in a turbulent boundary layer.

The characteristic vortex structures in the wall region during the early-turbulence stage ($T = 79$) are shown in figures 22(a, b). There is a striking difference between the sublayer structures existing at this stage and the horseshoe vortices of the five-spike stage. First, the strength of the streamwise vortices is now reduced to approximately $\frac{1}{5}$ of the mean spanwise vorticity and, secondly, their typical streamwise length has reached a value of $\lambda_z \approx 300$–400 in wall units. The typical length of spanwise vorticity is also elongated along x_1, whereas the correspondence between the spanwise locations of high concentrations of ω_x and ω_z is not as strong as in the previous stages. In figure 23 ω_x contours at the early-turbulence stage are shown in the vicinity of the lower wall. The existence of a fluctuating array of counter-rotation vortices covering the entire lower wall is apparent in this figure. In summary, the streamwise structures of the early-turbulence stage manifest a close resemblance to the characteristic near-wall structures of fully developed turbulence. Note that the main element of the organized structure of the near-wall turbulence is a system of counter-rotating streamwise vortices with $\lambda_x \approx 100$ and of strength about one order of magnitude less than the mean spanwise vorticity (Cantwell 1981). Hence, even though the Theodorsen-type horseshoe vortices seem to form the basic elements of late transition, the existence of these structures in the early-turbulence stage is not evidenced from the present results.

As we have noted before, the mechanism that is responsible for the generation of vorticity concentrations is explained as vortex stretching (and deformation) by the

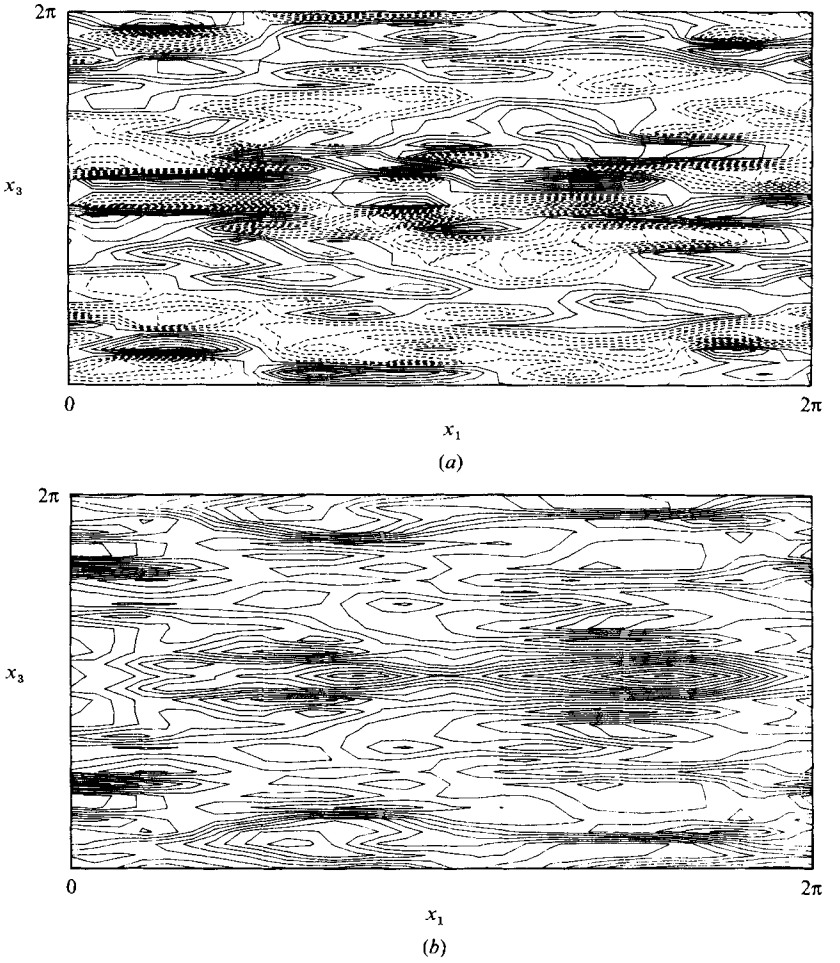

FIGURE 22. Vorticity contours in the (x_1, x_3)-plane at $T = 79$: (*a*) ω_x, contours from -1.2–1.2; (*b*) ω_z, contours from 0.9–6.6. Note the elongation to the vortex structures along x_1. Flow direction is from left to right.

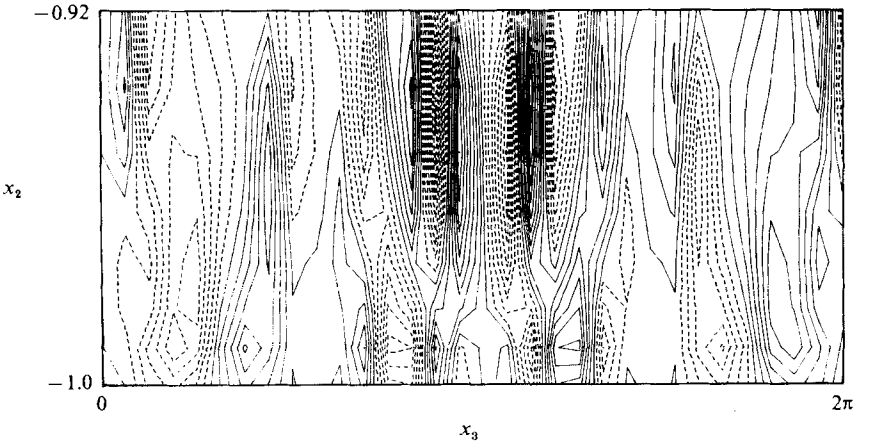

FIGURE 23. Contour plots of ω_x in the (x_1, x_2)-plane at $T = 79$ in the vicinity of the lower wall. Contours from -0.9–0.9. Flow direction is into the (x_2, x_3)-plane.

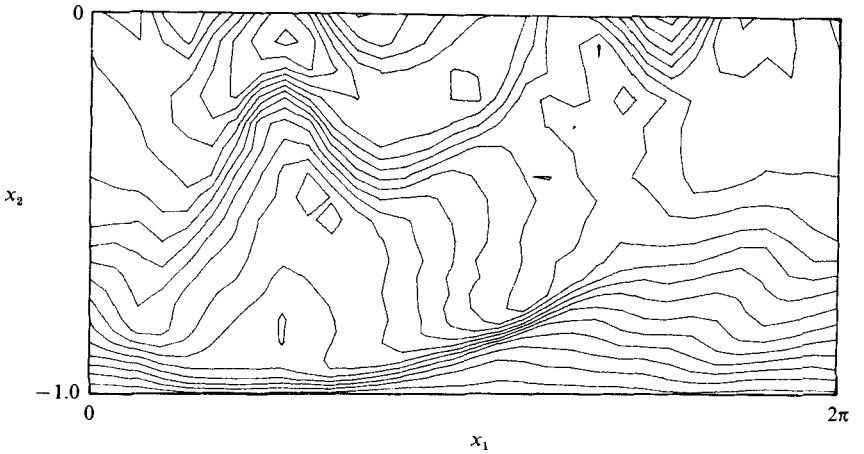

FIGURE 24. Contour plots of u_1 in the (x_1, x_2)-plane at $T = 27$. Contours from 0 to 1.02. Flow direction is from left to right.

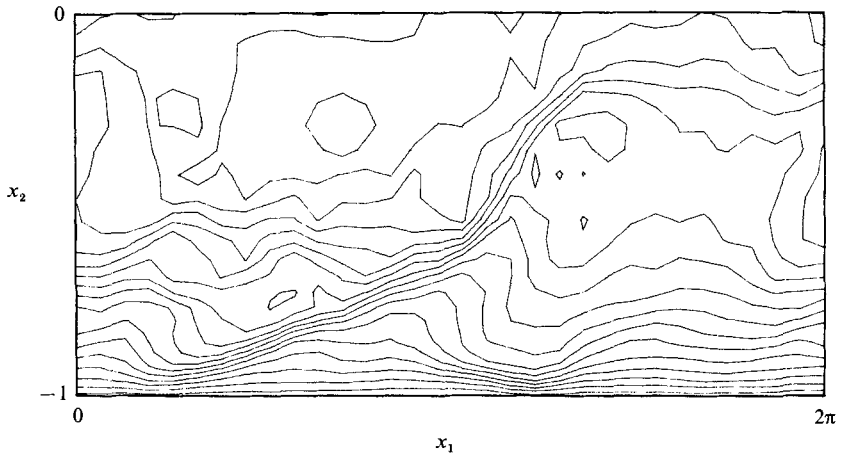

FIGURE 25. Contour plots of u_1 in the (x_1, x_2)-plane at $T = 44$. Contours from 0 to 1.02. Flow direction is from left to right.

mean flow. The stretched and deformed layer moves downstream with a translation velocity that induces a lower local velocity of the upstream edge of the vorticity layer than of its downstream edge (Komoda 1967). An examination of u_1 contours (figures 24 and 25) along with the approximate spanwise vorticity contours at $T = 27$ (figure 12*b*) and at $T = 44$ (figure 13*b*) in the (x_1, x_2)-plane clearly shows a similar trend. We observe that the nose of the vorticity layer is generally associated with higher velocities than the upstream region, and large variations of the local velocity exist within the layer.

Finally, in figures 26 and 27, normal velocity contours are shown in the (x_2, x_3)-plane at $T = 44$ and $T = 79$, corresponding to the multispike and early-turbulence stages respectively. These contours, plotted in the region between the lower wall ($x_2 = -1.0$) and $x_2 = -0.92$, display the evolution of alternating structures very similar to the characteristic streaklike near-wall structures observed in turbulent boundary layers (e.g. Kline *et al.* 1967) and recently simulated numerically in turbulent channel flows (Moin & Kim 1982).

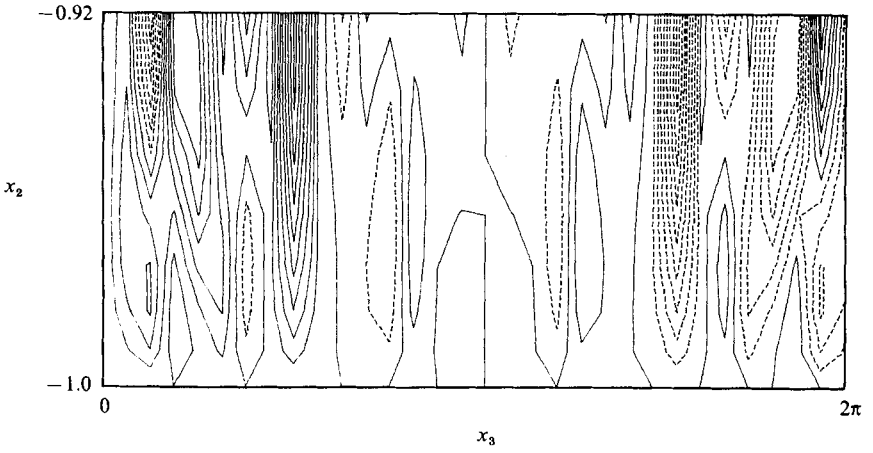

FIGURE 26. Contour plots of u_2 in the (x_2, x_3)-plane at $T = 44$. Contours from −0.08–0.08. Flow direction is into the (x_2, x_3)-plane.

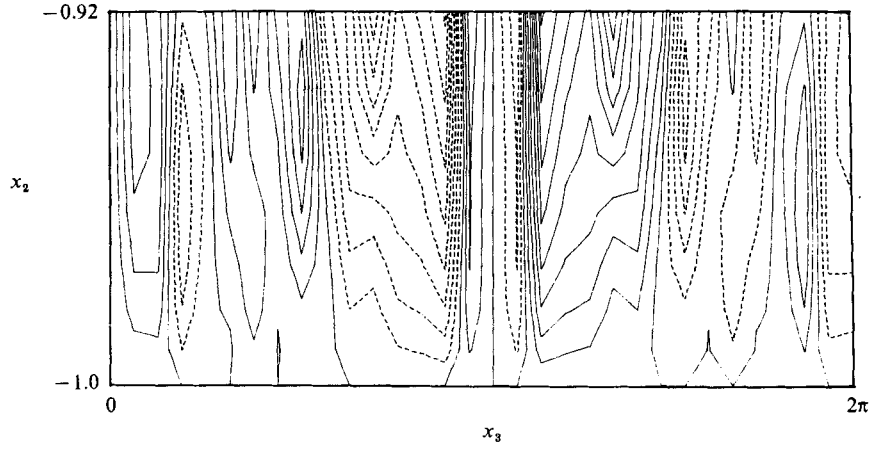

FIGURE 27. Contour plots of u_2 in the (x_2, x_3)-plane at $T = 79$. Contours from −0.06–0.06. Flow direction is into the (x_2, x_3)-plane.

4. Summary and concluding remarks

In this study, final stages of transition to turbulence in plane channel flow have been simulated by a direct numerical solution of the Navier–Stokes equations. It is found that, in spite of the limited resolution of the $32 \times 51 \times 32$ grid employed in the computations, the simulation is capable of reproducing most of the essential features of wall phenomena observed in the laboratory. Grid resolution in the x_1 and x_3 directions, along which the flow is periodic, is found to be adequate to capture the sequence of events that lead to early turbulence. Vorticity contours in the vicinity of the lower wall indicate formation of a system of horseshoe vortices with legs or extensions in the (x_1, x_3)-plane composed of counter-rotating streamwise vortex pairs. This picture is compatible with the observations of Hama & Nutant (1963) in boundary-layer transition. It is interesting to note that this vortex structure seems to be characteristic only of late transition. In the early-turbulence stage, however,

the vortex structures nearest the wall are not unlike the elongated streamwise vortex pairs typical of wall-bounded turbulent flows. Our findings are also in accord with the Benney–Lin (1960) theory, e.g. the present computations clearly depict frequency doubling of streamwise vorticity. It should be noted that the initial conditions used in this work are of the Benney–Lin type and consist of a vorticity field with a strong spanwise component and weak streamwise and transverse components. Therefore the question of the origin of streamwise vorticity and its precise relation to distortions of spanwise vorticity remain to be addressed in future work.

At later stages of the computation, transverse velocity contours indicate the formation of streaklike structures alternating in the spanwise direction. Typically, the spanwise characteristic length of these vortices, inferred from the spanwise variations of u_1, was found to be $\lambda_z \approx 115$; this is close to $\lambda_z = 100$ of fully developed wall turbulence. It was found that, during the later stages of transition, flow-field statistics indicate the formation of a laminar sublayer; however, the development of the logarithmic region and consequently the approach to fully developed turbulence is slow. This gradual approach to steady state is also reflected in the profiles of plane-averaged intensity and shear stress.

The main deficiency of this study stems inevitably from limited spatial resolution, and manifests itself in several ways. First, at later stages of the computation (e.g. past the early-turbulence stage), insufficient mesh resolution results in lower gradients of the mean velocity in the viscous sublayer. This, in turn, causes less turbulence production in the wall region, as evidenced by the absence of peaks in the intensity and shear-stress profiles close to the wall. Secondly, the finite cut-off wavenumbers along x_1 and x_3 prevent the formation of a fully turbulent wavenumber spectrum. This is not surprising when we consider that, in order to obtain self-sustaining (fully developed) turbulence, a direct numerical simulation requires a computational grid fine enough to resolve the smallest (dissipative–Kolmogorov) scales of motion. The ratio of the large scales to the Kolmogorov scales can be obtained via dimensional considerations, and reads $L/\eta = (Re_L)^{\frac{3}{4}}$. In the present work $(Re_L)^{\frac{3}{4}}$ is 241, and consequently a computational grid of $241 \times 241 \times 241$ is required to simulate self-sustaining turbulence at $Re = 1500$. The available resolution used in the present work, i.e. the $32 \times 51 \times 32$ grid, is adequate to simulate transition through the early-turbulence stage without significant pollution of the Fourier modes, as can be inferred from the one-dimensional spectra of the wall pressure (Biringen & Maestrello 1984). Simulation of transition beyond this stage and obtaining fully developed turbulence, however, necessitates the use of either higher grid resolution or the incorporation of a mechanism to account for subgrid-scale turbulence.

This work was supported by NASA/Langley Research Center under Grant NAG-1-228. The author is indebted to J. H. Ferziger, L. Maestrello, P. Moin and W. C. Reynolds for helpful discussions, and to P. J. Bobbitt and W. D. Harvey for their interest during the course of this work.

REFERENCES

Benney, D. J. & Lin, C. C. 1960 On the secondary motion induced by oscillations in a shear flow. *Phys. Fluids* **4**, 656.

Biringen, S. & Maestrello, L. 1984 Development of spot-like turbulence in plane channel flow. *Phys. Fluids* **27**, 318.

Cantwell, B. J. 1981 Organized motion in turbulent flow. *Ann. Rev. Fluid Mech.* **13**, 457.

CARLSON, D. R., WIDNALL, S. E. & PEETERS, M. F. 1982 A flow-visualization study of transition in plane Poiseuille flow. *J. Fluid Mech.* **121**, 487.

CRAIK, A. D. D. 1971 Non-linear resonant instability in boundary layers. *J. Fluid Mech.* **50**, 393.

FASEL, H., BESTEK, H. & SCHEFENACKER, R. 1977 Numerical simulation studies of transition phenomena in incompressible, two-dimensional flows. In *Laminar–Turbulent Transition: AGARD Conf. Proc.* 224, p. 14.

GEORGE, W. D. & HELLUMS, J. D. 1972 Hydrodynamic stability in plane Poiseuille flow with finite-amplitude disturbances. *J. Fluid Mech.* **12**, 1.

HAMA, F. R. & NUTANT, J. 1963 Detailed flow field observations in the transition process in a thick boundary layer. In *Proc. 1963 Heat Transfer and Fluid Mechanics Institute.* Stanford University Press.

HEAD, M. R. & BANDYOPADHYAY, P. 1981 New aspects of turbulent boundary-layer structure. *J. Fluid Mech.* **107**, 297.

HERBERT, T. 1981 Stability of plane Poiseuille flow – Theory and experiment. *Dept Engng Sci. and Mech., Virginia Poly. Inst. and State Univ. Rep.* VPI-E-21-35.

HERBERT, T. 1983 Secondary instability of plane channel flow to subharmomic three-dimensional disturbances. *Phys. Fluids* **26**, 871.

KAO, T. W. & PARK, C. 1970 Experimental investigations of the stability of channel flows. Part 1. Flow of a single liquid in a rectangular channel. *J. Fluid Mech.* **43**, 145.

KLEBANOFF, P. S., TIDSTROM, K. D. & SARGENT, L. M. 1962 The three-dimensional nature of boundary-layer instability. *J. Fluid Mech.* **12**, 1.

KLEISER, L. 1982 Spectral simulations of laminar–turbulent transition in plane Poiseuille flow and comparison with experiments. In *Proc. 8th Intl Conf. on Numerical Methods in Fluid Dynamics, Aachen* (ed. E. Krause). Lecture Notes in Physics, vol. 170, p. 280. Springer.

KLINE, S. J., REYNOLDS, W. C., SCHRAUB, F. A. & RUNSTADLER, P. W. 1967 The structure of turbulent boundary layers. *J. Fluid Mech.* **30**, 741.

KOMODA, H. 1967 Nonlinear development of disturbance in laminar boundary layer. *Phys. Fluids Suppl.* **10**, 87.

KOVASZNAY, L. S. G., KOMODA, H. & VASUDEVA, B. R. 1962 Detailed flow field in transition. In *Proc. 1962 Heat Transfer and Fluid Mech. Inst.*, p. 1.

MANSOUR, N. N., FERZIGER, J. H. & REYNOLDS, W. C. 1978 Large eddy simulation of a turbulent mixing layer. *Dept Mech. Engng, Stanford Univ. Rep.* TF-11.

MOIN, P. & KIM, J. 1982 Numerical investigation of turbulent channel flow. *J. Fluid Mech.* **118**, 341.

MOIN, P., REYNOLDS, W. C. & FERZIGER, J. H. 1978 Large eddy simulation of incompressible turbulent channel flow. *Dept Mech. Engng, Stanford Univ. Rep.* TF-12.

NISHIOKA, M., ASAI, M. & IIDA, S. 1980 An experimental investigation of the secondary instability. In *Laminar–Turbulent Transition* (ed. R. Eppler & H. Fasel), p. 37. Springer.

NISHIOKA, M., ASAI, M. & IIDA, S. 1981 Wall phenomena in the final stage of transition to turbulence. In *Transition and Turbulence* (ed. R. E. Meyer), p. 113. Academic.

ORSZAG, S. A. 1976 Turbulence and transition: A progress report. In *Proc. 5th Intl Conf. on Numerical Methods in Fluid Dynamics* (ed. A. I. van de Vooren & P. J. Zandbergen). Lecture Notes in Physics, vol. 59, p. 32. Springer.

ORSZAG, S. A. 1972 Comparison of pseudo spectral and spectral approximation. *Stud. Appl. Maths* **51**, 253.

ORSZAG, S. A. & KELLS, L. C. 1980 Transition to turbulence in plane Poiseuille and plane Couette flow. *J. Fluid Mech.* **96**, 159.

ORSZAG, S. A. & PATERA, A. T. 1981 Subcritical transition to turbulence in planar shear flows. *Phys. Rev. Lett.* **45**, 989.

PERRY, A. E., LIM, T. T. & TEH, E. W. 1981 A visual study of turbulent spots. *J. Fluid Mech.* **104**, 381.

REYNOLDS, W. C. 1967 A Fortran IV program for solution of the Orr–Sommerfeld equation. *Dept Mech. Engng, Stanford Univ. Rep.* FM-4.

SMITH, C. R. & METZLER, S. P. 1983 The characteristics of low-speed streaks in the near-wall region of a turbulent boundary layer. *J. Fluid Mech.* **129**, 27.

SMITH, C. R. & SCHWARTZ, S. R. 1983 Observation of streamwise rotation in the near-wall region of a turbulent boundary layer. *Phys. Fluids* **26**, 641.

TANI, I. 1969 Boundary layer transition. *Ann. Rev. Fluid Mech.* **1**, 169.

TENNEKES, H. & LUMLEY, J. L. 1972 *A First Course in Turbulence.* MIT Press.

THEODORSEN, T. 1955 The structure of turbulence. In *50 Jahre Grenzschichtforschung*, p. 55. Vieweg.

WRAY, A. & HUSSAINI, M. Y. 1984 Numerical experiments in boundary-layer stability. *Proc. R. Soc. Lond.* A **392**, 373.